The comments of RC1

1、Reply to the comment 1：

1.1 Comments from Referees

The technique used in the data processing is the Full Rank Matrix (FRAM) Small Baseline Subset InSAR (SBAS) time-series analysis, but the methodis not clear described in the main text. More details of the technique should be added in Section 3.2.

1.2 Author's response

According to your suggestion, we will add the details of the technique in section 3.2. As follows:

The main steps of the FRAM-SBAS (Full Rank Matrix-Small Baseline Subset InSAR) method are as follows:

Firstly, the principle of interferogram generation is based on a specific time baseline and space baseline, and the appropriate redundant interferogram is selected to maximize the interferogram coherence. The main constraints are

$$\begin{aligned} &\left|\Delta B_{\perp}\right| < B_{\perp thr} \\ &\left|\Delta t\right| < t_{thr} \\ &\left|\Delta DC\right| < DC_{thr} \end{aligned} \qquad (1)$$

where $\Delta B_{\perp}$ is the vertical baseline of data interference pairs, Δt is the time baseline and ΔDC is the Doppler frequency difference.

Secondly, coherence points are selected. The coherence point is selected based on the principle of full rank matrix, which effectively improves the quality of coherent point selection and provides the basis for subsequent least squares inversion. By constructing a single set interferogram network, each point can construct the matrix described by Equation 1, where A is an $M * N$ dimensional matrix, M is the number of interferograms, and N is the number of images. For any pixel in any interferogram, the coherence is greater than a certain threshold, and the -1 and 1 flags can be set at the corresponding positions of the matrix A of Equation 1. For example, the first interferogram consists of the first image and the third image; that is, $\delta_{\phi 1}=\phi_3-\phi_1$. If the interference of a certain point in the interferogram satisfies the conditions, then the corresponding position are $A_{11}=-1$ and $A_{13}=1$, and the remaining positions of the first line are 0. Similarly, in the second interferogram, if the coherence of the point in one of the interferograms is less than the coherence threshold, the diversion is set to zero. All interferograms are considered to obtain each point pair matrix, and then the rank of each matrix is determined. If the matrix is full rank, the point is selected as the coherence point. The method can be used to select points that are coherent in the time series and coherent in the partial time interval but the interference network is connected, thereby increasing the number and precision of the coherent points.

$$A=\begin{bmatrix} -1 & 0 & 1 & \cdots & 0 & 0 & 0 \\ 0 & -1 & 1 & \cdots & 0 & 0 & 0 \\ & & \cdots\cdots\cdots\cdots & & & & \\ & & \cdots\cdots\cdots\cdots & & & & \\ 0 & 0 & 0 & \cdots & -1 & 1 & 0 \\ 0 & 0 & 0 & \cdots & -1 & 0 & 1 \end{bmatrix} \quad (2)$$

Thirdly, discrete point phase unwrapping is performed. In the FRAM-SBAS method, discrete coherence point data are resampled onto a regular Cartesian grid and phase unwrapping is performed using a network flow method. Then, the phase jump is checked according to the closed ring residual method, and the jump phase is corrected for the jump region.

Fourthly, orbital and atmospheric error removal is performed. The orbit error removal is performed using the network method proposed by Biggs et al. (2007). The atmospheric error is divided into long-wavelength atmospheric delay error and turbulent atmospheric delay error and terrain-related atmospheric delay error. The three errors are removed using the network methods. Traditional atmospheric delay phase (APS) estimates are based on a single interferogram (Ferretti et al., 2001). The atmospheric phase in the interferogram is the difference in atmospheric phase delay between the sub-image and the main image. If one of the two images is used to generate other interferograms, the phase delay signal on the image is also passed to the other interferograms, which also makes a correlation between the two interferograms. In this paper, we will use the network method to estimate the atmospheric delay error of each image acquisition time and then use these estimates to obtain the delay error of a single moment to reconstruct the atmospheric delay error of each interferogram.

After removal of the DEM error and the deformation phase, it can be assumed that the residual phase is mainly caused by the atmosphere. Suppose $\delta\varphi_j(x,y)$ represents the residual phase value at (x,y) on the jth interferogram and that $\varphi(t_A,x,y)$ and $\varphi(t_B,x,y)$ represent the phase values of the imaging moments t_A and t_B at (x,y), respectively. Each interferogram can be expressed by Equation (3):

$$\delta\varphi_j(\mathrm{x},\mathrm{y})=\varphi(t_B,x,y)-\varphi(t_A,x,y) \quad (3)$$

Based on a short baseline set network, we can construct equations such as (4):

$$\boldsymbol{\delta\varphi = A*\varphi} \quad (4)$$

where $\boldsymbol{A}$ represents the $M*N$ matrix. The element A_{kl} of the matrix $\boldsymbol{A}$ is defined according to the following rules: If $l=t_B$, then $A_{kl}=1$; if $l=t_A$, then $A_{kl}=-1$; otherwise, $A_{kl}=0$. $\boldsymbol{\delta\varphi}$ is a known vector of M dimension, representing the number of interferograms M; $\boldsymbol{\varphi}$ is an N-dimensional unknown vector representing the atmospheric phase values of N imaging moments. Equation (4) can be rewritten as follows:

$$\begin{bmatrix} \delta\varphi_1(x,y) \\ \vdots \\ \delta\varphi_k(x,y) \end{bmatrix} = \begin{bmatrix} -1 & 0 & 1 & & \\ & \ddots & & \ddots & \\ & & 0 & -1 & 1 \end{bmatrix} \begin{bmatrix} \varphi^{t_0}(x,y) \\ \vdots \\ \varphi^{t_1}(x,y) \end{bmatrix} \quad (5)$$

where $\delta\varphi_k(x,y)$ represents the residual phase of interferogram k and the corresponding position is (x, y).

Since the matrix $\boldsymbol{A}$ is the rank-deficient matrix, a unique solution cannot be obtained. Generally, the singular value decomposition (SVD) method can be used to solve the solution and the atmospheric delay at each moment is obtained; then, the phase value of each interferogram is simulated by using Equation (5). In the calculation of the variance of the residual phase of each interferogram, if the interferogram has the lowest atmospheric variance, the atmospheric phase of the interferogram is assumed to be zero. This constraint is added to Equation (5) to calculate the atmospheric delay phase of all other image acquisition moments (Li et al., 2014).

Fifthly, the deformation result is obtained. The interference pattern is settled using the least squares method to obtain the deformation results of the study area.

1.3 Author's changes in manuscript.

The contents of the response have been updated to the Section 3.2 (page 5 to page 7).

2、Reply to the comment 2：

2.1 Comments from Referees

Comment 2: The deformation result from the study is not validated. And what is the precision or accuracy of the derived deformation?

2.2 Author's response

In Section 4.1, the comparison between the results of this paper and the results of others is added, and the reliability of the results is verified. As follows:

In this paper, the SAR data from 2003 to 2012 are analyzed. It is concluded that during the construction of the Qinghai-Tibet Railway, the linear variable along the railway was approximately 10 mm/yr. After the completion of the traffic, the linear variable along the railway was 4-8 mm/yr. Li et al. (2012) used SBAS technology to analyze the ENVISAT ASAR data from 1997 to 2010 in the vicinity of Yangbajing-Dangxiong of the Qinghai-Tibet Railway. It was found that the settlement rate near the railway was 2 mm/yr, and the impact of frozen soil was approximately 10 mm/yr. Zhang et al. (2017) used Sentinel-1 data to analyze the deformation variables of the Qinghai-Tibet Railway during the period of 2014-2016 in the Qinghai-Tibet Plateau. It is concluded that the settlement rate of the Qinghai-Tibet Railway is approximately -10 mm/yr and the settlement rate of the rail-stabilized area is approximately -5 mm/yr. Ma et al. (2011) and Dong et al. (2013) found that the overall settlement rate of the Qinghai-Tibet Railway subgrade is <10 mm/yr. At the junction of the

fracture, we verified this finding with GPS, and the GPS result was highly consistent with the deformation field acquired by InSAR. Chen et al. (2012) used C- and L-band small baseline SAR interferometry to analyze the interaction between permafrost and infrastructure along the Qinghai-Tibet Railway, and the results showed surface motions along the embankment primarily in the range of - 20 to + 20 mm/yr.

2.3 Author's changes in manuscript.

The contents of the response have been updated to the Section 4.1 (page 8 to page 9).

3、Reply to the comment 3：

3.1 Comments from Referees

Comment 3: The reference style in P2/L1 and the following texts should be rewritten under the style of NHESSD, for example, “Xiaolei Lv et al., (2003)” should be changed to “Lv et al., (2003)”.

3.2 Author's response

According to your suggestion, the references formats of the full text have been modified on the basis of your example.

3.3 Author's changes in manuscript.

The contents of the response have been updated to the full manuscript (page 1 to page 10).

4、Reply to the comment 4：

4.1 Comments from Referees

Comment 4: P3/L7, global positioning systems (GPS) -> Global Positioning Systems (GPS).

4.2 Author's response

According to your suggestion, we changed the global positioning systems (GPS) to Global Positioning Systems (GPS).

4.3 Author's changes in manuscript.

The contents of the response have been updated to the Section 2 (line 5 - 6 of page 3).

5、Reply to the comment 5：

5.1 Comments from Referees

Comment 5: P3/L13-21, Need some references.

5.2 Author's response

According to your suggestion, we will add references in section 2. As follows:

The Qinghai-Tibet Railway is a high-elevation railway that connects Xining (Qinghai Province) to Lhasa (Tibet Autonomous Region) (Figure 1). The Qinghai-Tibet Railway and other national key projects that cross multiple active blocks and faults are vulnerable to earthquakes and other disasters (Chen et al., 2018; Wu et al., 2016). Thus, monitoring the deformation of these projects is particularly important. InSAR and GPS are efficient techniques for monitoring the crustal deformation of Qinghai-Tibet blocks (Zhang et al., 2017).

The Qinghai-Tibet Railway, highway, transmission line and other national key projects, with their ancillary studies, have the characteristics of strong correlations and continuous long-distance distributions. It is important to understand how to use these features to monitor the deformation of a long, linear region and reveal the movement of the Qinghai-Tibet Plateau block patterns with the deformations of these major project networks.

The Lhasa-Nagqu section of the railway is located at the bottom of the southern valley of Nyainqentanglha Mountain in the central part of the Lhasa block (Jiang et al., 2018). In general, this section is north trending, and the Qinghai-Tibet Highway and Lhasa River pass through the area. Figure 2 shows the study area, and the base map is derived from a digital elevation model (DEM). The terrain in the area is undulating, with the Nyainqentanglha Mountain Range in the northwest, a mountainous area in the southeast, and the Yangbajing-Damxung Basin in the middle of the region (Wu et al., 2018). The terrain is flat, the Qinghai-Tibet Railway and Qinghai-Tibet Highway pass through the basin, and the vegetation along the railway is dense. Wetlands and low-lying regions are widely distributed, and the frozen soil in a long segment of the area contains abundant ice (Li et al., 2012). The study area is in a midlatitude region, and the land types mainly include glaciers, snow, bare rock and other land types. In this area, the Bengco fault lies across the railway; therefore, it is also important to study whether the movement of the Bengco fault affects the stability of the railway.

5.3 Author's changes in manuscript.

The contents of the response have been updated to the Section 2 (page 3 to page 4).

6、Reply to the comment 6：

6.1 Comments from Referees

Comment 6: P3/L29-P4/9,The tense of these paragraphs should be the past tense.

6.2 Author's response

According to your suggestion, we changed the paragraph tense in section 3.1. As follows:

The TerraSAR-X data were acquired in stripmap mode with an incidence angle range of 39°-40° at HH polarization. The potential of the X-band data for detecting higher deformation gradients compared to that of other sensors arises from the high spatial and temporal resolutions of these data. Nevertheless, the coverage of the stripmap mode data is too small to study long, linear engineering projects. Therefore, in this paper, the C-band ASAR data and TerraSAR-X data were used in combination to analyze the stability of the Qinghai-Tibet Railway. The TerraSAR-X data were selected to verify the accuracy of the ASAR

T405 data results over the first segment of the railway in Yangbajain, and the ASAR T133 data were used to analyze the deformation of the railway near the Nagqu area because the ASAR T405 data could not cover this area completely, and the ASAR T133 data could also verify the accuracy of the ASAR T405 data results over the Nagqu area. The data coverage is shown in Figure 2 with the blue dotted line.

The ASAR T405 data were acquired from August 2003 to September 2010, but there were no data for 2016; therefore, we processed the data in three stages (2003-2005, 2007, and 2008-2010). The ASAR T133 data were acquired from November 2007 to August 2010. The TerraSAR-X data were acquired from December 2011 to November 2012.

6.3 Author's changes in manuscript.

The contents of the response have been updated to the Section 3.2 (page 4 to page 5).

7、Reply to the comment 7：

7.1 Comments from Referees

In Figure 4, interferograms -> interferogram

7.2 Author's response

According to your suggestion, we changed the interferograms to interferogram in figure 4. As follows:

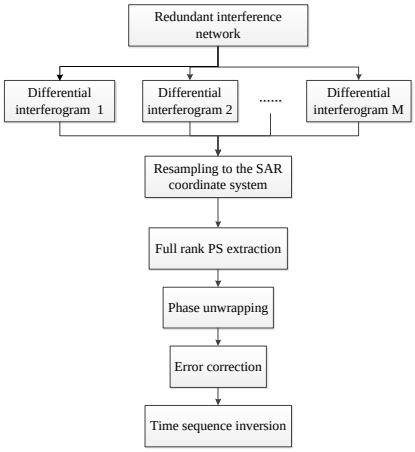

7.3 Author's changes in manuscript.

The contents of the response have been updated to the figure 4 (page 17).

8、Reply to the comment 8：

8.1 Comments from Referees

Comment 8: The Figures 5, 6 and 7 can be combined as one figure.

8.2 Author's response

According to your suggestion, we combined the figure 5,6 and 7 as figure 5. As follows:

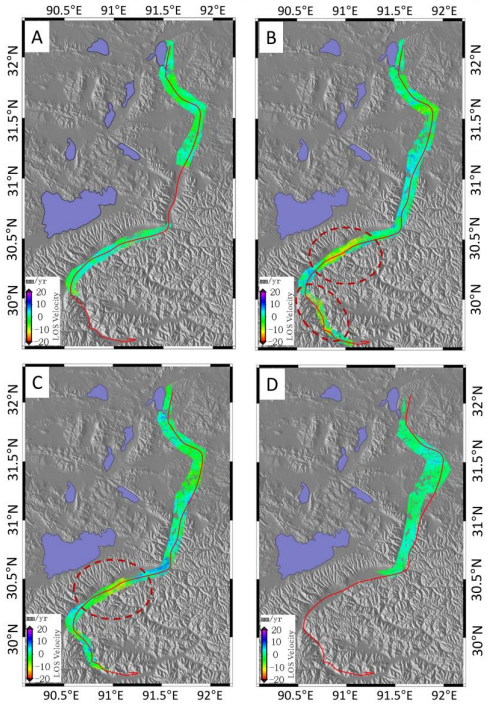

8.3 Author's changes in manuscript.

The contents of the response have been updated to the figure 5 (page 18).

References

Chen, T., Ma, W., and Zhou, G.: Numerical analysis of ground motion characteristics in permafrost regions along the

Qinghai-Tibet Railway, Cold Regions Science & Technology, 148, 88-95, https://doi.org/10.1016/j.coldregions.2018.01.016, 2018.

Dong, C. H., and Zhao, X. Q.: Analysis on subgrade deformation features and influence factors in permafrost regions on Qinghai-Tibet Railway, Railway Standard Design, 6: 5-8, 2013.

Jiang, Y., Gao, Y., Dong, Z. B., Liu, B. L., and Zhao, L.: Simulations of wind erosion along the Qinghai-Tibet Railway in north-central Tibet, Aeolian Research, 32, 192-201, https://doi.org/10.1016/j.aeolia.2018.03.006, 2018.

Li, S. S.: The study of using SBAS to monitor the Motion of the frozen soil along Qinghai-Tibet railway, Central south university, 2012

Ma, W., Liu, D., and Wu, Q. B.: Monitoring and analysis of embankment deformation in permafrost regions of Qinghai-Tibet Railway, Rock Mechanics, 29(3) : 571-580, 2008.

Ma, W., Mu, Y. H., and Wu, Q. B.: Characteristics and mechanisms of embankment deformation along the Qinghai-Tibet Railway in permafrost regions, Cold Regions Science and Technology, 67(3) : 178-186, 2011.

Wu, Z. J., Ma, W., Chen, T., and Wang, L.: Dynamic Stability Analysis of Embankment Along the Qinghai-Tibet Railroad in Permafrost Regions, Environmental Vibrations and Transportation Geodynamics, 757-766, Doi: 10.1007/978-981-10-4508-070, 2016.

Zhang, Z. J.: Research on Qinghai-Tibet Permafrost Environment and Engineering using High Resolution SAR Images, Institute of Remote Sensing and Digital Earth, Chinese Academy of Science, 2017.

The comments of RC2

1、Reply to the comment 1：

1.1 Comments from Referees

Comment 1: I would like to suggest the authors add a short description of the used methodology with a particular emphasis on the estimation and removal of APS.

1.2 Author's response

According to your suggestion, we will add the details of the technique in section 3.2. As follows:

Traditional atmospheric delay phase (APS) estimates are based on a single interferogram (Ferretti et al., 2001). The atmospheric phase in the interferogram is the difference in atmospheric phase delay between the sub-image and the main image. If one of the two images is used to generate other interferograms, the phase delay signal on the image is also passed to the other interferograms, which also makes a correlation between the two interferograms. In this paper, we will use the network method to estimate the atmospheric delay error of each image acquisition time and then use these estimates to obtain the delay error of a single moment to reconstruct the atmospheric delay error of each interferogram.

After removal of the DEM error and the deformation phase, it can be assumed that the residual phase is mainly caused by the atmosphere. Suppose $\delta\varphi_j(x,y)$ represents the residual phase value at (x,y) on the jth interferogram and that $\varphi(t_A,x,y)$ and $\varphi(t_B,x,y)$ represent the phase values of the imaging moments t_A and t_B at (x,y), respectively. Each interferogram can be expressed by Equation (3):

$$\delta\varphi_j(\mathrm{x},\mathrm{y}) = \varphi(t_B,x,y) - \varphi(t_A,x,y) \quad (3)$$

Based on a short baseline set network, we can construct equations such as (4):

$$\boldsymbol{\delta\varphi = A * \varphi} \quad (4)$$

where $\boldsymbol{A}$ represents the $M * N$ matrix. The element A_{kl} of the matrix $\boldsymbol{A}$ is defined according to the following rules: If $l = t_B$, then $A_{kl} = 1$; if $l = t_A$, then $A_{kl} = -1$; otherwise, $A_{kl} = 0$. $\boldsymbol{\delta\varphi}$ is a known vector of M dimension, representing the number of interferograms M; $\boldsymbol{\varphi}$ is an N-dimensional unknown vector representing the atmospheric phase values of N imaging moments. Equation (4) can be rewritten as follows:

$$\begin{bmatrix} \delta\varphi_1(x,y) \\ \vdots \\ \delta\varphi_k(x,y) \end{bmatrix} = \begin{bmatrix} -1 & 0 & 1 & & \\ & \ddots & & \ddots & \\ & & 0 & -1 & 1 \end{bmatrix} \begin{bmatrix} \varphi^{t_0}(x,y) \\ \vdots \\ \varphi^{t_N}(x,y) \end{bmatrix} \quad (5)$$

where $\delta\varphi_k(x,y)$ represents the residual phase of interferogram k and the corresponding position is (x, y).

Since the matrix $\boldsymbol{A}$ is the rank-deficient matrix, a unique solution cannot be obtained. Generally, the singular value decomposition (SVD) method can be used to solve the solution and the atmospheric delay at each moment is obtained; then, the phase value of each interferogram is simulated by using Equation (5). In the calculation of the variance of the residual phase of each interferogram, if the interferogram has the lowest atmospheric variance, the atmospheric phase of the interferogram is assumed to be zero. This constraint is added to Equation (5) to calculate the atmospheric delay phase of all other image acquisition moments (Li et al., 2014).

1.3 Author's changes in manuscript.

The contents of the response have been updated to the Section 3.2 (page 6 to page 7).

2、Reply to the comment 2：

2.1 Comments from Referees

Comment 2: Some minor changes are required concerning English style.

2.2 Author's response

According to your suggestion, when the next manuscript is uploaded, the English style of the full text will be revised.

2.3 Author's changes in manuscript.

The contents of the response have been updated to the full-text.

3、Reply to the comment 3：

3.1 Comments from Referees

Comment 3: Reference to the literature is not adequate but it must be improved by searching for the most recent publications on the InSAR field. Also, the original SBAS paper of Berardino et al. has not been cited. Also, several other SBAS-like methods have been designed and presented in the literature.

3.2 Author's response

According to your suggestion, we will add the reference of the InSAR and SBAS. As follows:

In view of the drawbacks of D-InSAR technology affected by the temporal baseline and spatial displacement, many scholars have proposed new technologies, such as InSAR time series analysis methods, to obtain better settlement detection results. The main time series analysis methods of InSAR include the Permanent Scatter Interferometry SAR (PS-InSAR) method (Ferreti et al., 2000, 2001; Rosi et al., 2017; Yang et al., 2018), the Small Baseline Subset InSAR (SABS-InSAR) method (Berardino et al., 2002; Dong at al., 2014; Li et al., 2015; Corsetti et al., 2018) and the Stacking method (Lundgren et al., 2001; Chang et al., 2011; Dai et al., 2018).

Reference:

Ferretti, A.: Nonlinear subsidence rate estimation using permanent scatters in differential SAR interferometry, IEEE Transactions on Geoscience & Remote Sensing, 38(5), 2202-2212, doi: 10.1109/36.868878, 2000.

Ferretti, A.: Permanent scatterers in SAR interferometry, IEEE Transactions on Geoscience & Remote Sensing, 39 (1), 8-20, doi: 10.1109/36.898661, 2001.

Rosi, A., Tofani, V., Tanteri, L., Tacconi, S. C., Agostini, A., Catani, F., and Casagli, N.: The new landslide inventory of Tuscany (Italy) updated with PS-InSAR: geomorphological features and landslide distribution, Landslides, 15(1), 5-19, doi: 10.1007/s10346-017-0861-4, 2017 .

Yang, C., Lu, Z., Zhang, Q., Zhao, C. Y., Peng, J. B., and Ji, L. Y.: Deformation at longyao ground fissure and its surroundings, north China plain, revealed by ALOS PALSAR PS-InSAR, International Journal of Applied Earth Observation and Geoinformation, 67, 1-9, https://doi.org/10.1016/j.jag.2017.12.010, 2018.

Berardino, P., Fornaro, G., Lanari, R., and Sansosti, E.: A New Algorithm for Surface Deformation Monitoring Based on Small Baseline Differential SAR Interferograms, Geoscience and Remote Sensing, IEEE Transactions, 40(11), 2375-2383, doi: 10.1109/TGRS.2002.803792, 2002.

Corsetti, M., Fossati, F., Manunta, M., and Marsella, M.: Advanced SBAS-DInSAR technique for controlling large civil

infrastructures: An Application to the Genzano di Lucania Dam, Sensors, 18(7), doi: 10.3390/s18072371, 2018.

Dong, . (2014). Time-series analysis of subsidence associated with rapid urbanization in shanghai, china measured with sbas insar method. Environmental Earth Sciences, 72(3), 677-691.

Dong S. C., Samsonov, S., Yin, H. W., Ye, S. J., and Cao, Y. R.: Time-series analysis of subsidence associated with rapid urbanization in Shanghai, China measured with SBAS InSAR method, Environmental Earth Sciences, 72(3), 677-691, doi: 10.1007/s12665-013-2990-y, 2014.

Lundgren, P., Usai, S., Sansoti, E., Lanari, R., Tesauro, M., Fornaro G., and Berardino, P.: Modelling surface deformation observed with synthetic aperture radar interferometry at Campi Flegrei caldera, Journal of Geophysical Research, 106 (B9), 19355–19366, doi: 10.1029/2001jb000194, 2001.

Chang, Z. Q., Liu, X. M., Xue, T. F., and Yang, R. R.: Investigating ground subsidence in Beijing by using interferogram stacking InSAR, IEEE International Conference on Spatial Data Mining & Geographical Knowledge Services, IEEE, doi: 10.1109/ICSDM.2011.5969068, 2011.

Dai, K. R., Liu, G. X., Li, Z. H., Ma, D. Y., Wang, X. W., Zhang, B., Tang, J., and Li, G. Y.: Monitoring Highway Stability in Permafrost Regions with X-band Temporary Scatterers Stacking InSAR, Sensors, 18(6), 1-17, doi: 10.3390/s18061876, 2018.

3.3 Author's changes in manuscript.

The contents of the response have been updated to the Section 1 and the References (line 23-28 of page 2 and page 11-15).

The minor issues of editor decision

1、Reply to the issue 1：

1.1 Issues from editor decision

Issue 1: please have a complete check of the English language by a native speaker

1.2 Author's response

According to your suggestion, when the next manuscript is uploaded, the English language was checked by a native speaker.

1.3 Author's changes in manuscript.

The contents of the response have been updated to the full-text.

2、Reply to the issue 2：

2.1 Issues from editor decision

Issue 2: please add more references related to previous case studies of the application of InSAR to the monitoring of lifelines and transportation networks. There are many of them in the recent literature and a comparison with your own work would be advisable.

2.2 Author's response

According to your suggestion, we will add more references related of the application of InSAR to the monitoring of lifelines and transportation networks in section 1. As follows:

Because the lifelines and transportation networks of railways and highways are long, linear projects, certain requirements must be met in the detection and analysis of such objects: First, large area coverage is necessary because the lifelines and transportation networks have different directions and unified reference data are needed for monitoring, requiring large-scale synchronous measurement. Second, the lifeline serves the people over a long time and requires long-term, near real-time monitoring. The traditional geodetic deformation monitoring methods are mainly based on leveling and Global Positioning System (GPS) approaches. Traditional leveling is limited to discrete points on fixed routes. This approach is time consuming and expensive, so it is difficult to use for real-time monitoring. Although GPS technology can achieve high-precision monitoring, it is subject to the density of GPS points. The development of sequential InSAR technology provides a feasible technical means for real-time and long-term monitoring of long-standing linear engineering projects. At present, there are many studies on the application of InSAR technology to lifelines and transportation networks (Hung et al., 2010; Shan et al., 2012; Chen et al., 2012; Qin et al., 2016; Hoope et al., 2014; Wang et al., 2017; Yu et al., 2013). The French SNCF Institute (2008) used TS-DInSAR technology to analyze the deformation along the Paris-Amsterdam high-speed railway and verified the feasibility of this method. Gatti et al. (2010) used PS-InSAR technology to analyze the deformation of a railway in Italy over three years, which further proved the applicability of time series InSAR technology. Daniel et al. (2018) used InSAR technology to monitor the changes in highway bridges, which verified the feasibility of InSAR technology for monitoring lifelines and other facilities. Xing et al. (2018) improved the technical accuracy of PS-InSAR by installing angular reflectors, but the installation of angular reflectors requires manpower and materials and depends on the amount of SAR data generated by PS-InSAR technology.

2.3 Author's changes in manuscript.

The contents of the response have been updated to the Section 1 and the References (line 1-18 of page 3 and page 11-15).

InSAR Technique Applied to the Monitoring of the Qinghai-Tibet Railway

Qingyun Zhang[1,2], Yongsheng Li[2], Jingfa Zhang[2], Yi Luo[2]

[1]The first Monitoring and Application Center, China Earthquake Administration, Tianjin, China.
[2]Key Laboratory of Crustal Dynamics, Institute of Crustal Dynamics, China Earthquake Administration, 100085, Beijing

Correspondence to: Yongsheng Li (liyongsheng0217@163.com)

Abstract. The Qinghai-Tibet Railway is located on the Qinghai-Tibet Plateau and is the highest-altitude railway in the world. With the influence of human activities and geological disasters, it is necessary to monitor ground deformation along the Qinghai-Tibet Railway. In this paper, Advanced Synthetic Aperture Radar (ASAR) (T405 and T133) and TerraSAR-X data were used to monitor the Lhasa-Nagqu section of the Qinghai-Tibet Railway from 2003 to 2012. The data period covers the time before and after the opening of the railway (total of ten years). This study used a new analysis method (Full Rank Matrix (FRAM) Small Baseline Subset InSAR (SBAS) time-series analysis) to analyze the Qinghai-Tibet Railway. Before the opening of the railway (from 2003 to 2005), the Lhasa-Nagqu road surface deformation was not obvious, with a maximum deformation of approximately 5 mm/yr; in 2007, the railway was completed and opened to traffic, and the resulting subsidence of the railway in the district of Damxung was obvious (20 mm/yr). After the opening of the railway (from 2008 to 2010), the Damxung segment included a considerable area of subsidence, while the northern section of the railway was relatively stable. The results indicate that FRAM-SBAS technology is capable of providing comprehensive and detailed subsidence information regarding railways with millimeter-level accuracy. An analysis of the distribution of geological hazards in the Damxung area revealed that the distribution of the subsidence area coincided with that of the geological hazards, indicating that the occurrence of subsidence in the Damxung area was related to the influence of surrounding geological hazards and faults. Overall, the peripheral surface of the Qinghai-Tibet Railway is relatively stable but still needs to be verified with real-time monitoring to ensure that the safety of the railway is maintained.

1 Introduction

The Qinghai-Tibet Railway is located on the Qinghai-Tibet Plateau, with a total length of more than 1,100 km, of which 632 km is within a permafrost region. This railway is the highest-elevation railway in the world and the longest railway crossing over a permafrost region (Han et al., 2010). The key to the success or failure of the Qinghai-Tibet Railway lies in the roadbed, and the key to the success or failure of the roadbed lies in the permafrost. In particular, under global warming and the impacts of human activities and other factors, the stability of the railway roadbed in permafrost regions is facing great challenges (Wu

et al., 2008; Liu et al., 2000; Wu et al., 2004). Permafrost is very sensitive to disturbance from external factors; the temperature increase decreases the strength of the frozen soil, the bearing capacity of the frozen soil is reduced, and the ability to resist load is reduced (Wu et al., 2005). Moreover, the higher the ice content in the frozen soil is, the greater the extent of settlement after the frozen soil thaws. The Qinghai-Tibet Railway subgrade project adopted the design concept of active cooling (Cheng et al., 2003), based on the assumption of a stable substrate. During the construction of the Qinghai-Tibet Railway, the differential settlement and the countermeasures employed in the road and bridge transition section in the permafrost region were studied in an experiment (Liu et al., 2004); countermeasures were proposed to address the differential settlement, but there are many bridges and the geological condition of the permafrost region is complex (Jin et al., 2008; Zhao et al., 2010). Therefore, the stability of the permafrost under the Qinghai-Tibet Railway is related to the normal operation and safety of railway.

In the past, investigations and monitoring of deformation of the Qinghai-Tibet Plateau mainly relied on field work (Welk, 1997; Brown et al., 2000; Ma et al., 2011), but the harsh natural conditions of certain areas of the Qinghai-Tibet Plateau led to heavy workloads and substantially increased the difficulty of performing traditional methods for measuring and analyzing deformation (Hu et al., 2007; Zhang et al., 2006). Therefore, it is necessary to explore a wide range of unattended, long-term, continuous methods for analyses of the deformation of the Qinghai-Tibet Railway. The development of interferometric synthetic aperture radar (InSAR) technology provides technical support for research on railway lifelines and transportation networks.

Surface deformation monitoring is one of the most advantageous applications of InSAR technology. As far as the research and development of methods and techniques are concerned, InSAR technology has been improved from the use of a small amount of single-phase SAR data to analyzing time series and processing multiphase and multisource data. Differential InSAR (D-InSAR) technology has been developed on the basis of InSAR technology. Grabriel et al. (1989) first used D-InSAR technology to monitor surface deformation, and the level of accuracy was maintained at the centimeter level. In subsequent decades, D-InSAR technology has been widely used in surface, volcanic deformation, and seismic displacement monitoring. In view of the drawbacks of D-InSAR technology affected by the temporal baseline and spatial displacement, many scholars have proposed new technologies, such as InSAR time series analysis methods, to obtain better settlement detection results. The main time series analysis methods of InSAR include the Permanent Scatter Interferometry SAR (PS-InSAR) method (Ferreti et al., 2000, 2001; Rosi et al., 2017; Yang et al., 2018), the Small Baseline Subset InSAR (SABS-InSAR) method (Berardino et al., 2002; Dong at al., 2014; Li et al., 2015; Corsetti et al., 2018) and the Stacking method (Lundgren et al., 2001; Chang et al., 2011; Dai et al., 2018). InSAR technology in China developed later but has also achieved good research results. Wang et al. (2000) used radar data to analyze the seismic deformation field and promote the development of D-InSAR technology in China. Li et al. (2009) improved the Atmospheric Phase Screen (APS) estimation algorithm on the basis of the traditional InSAR short baseline analysis method and proposed the InSAR time series (TS) + atmospheric estimation model (AEM) method to obtain good application results. Li et al. (2015, 2016) proposed improved methods for identifying errors

批注 [z1]: Reply to the comment 3 of RC1

批注 [z2]: Reply to the comment 3 of RC2

during phase unwrapping and correcting InSAR technology and advanced sequential InSAR analysis methods, and the study obtained very good results in practical applications.

Because the lifelines and transportation networks of railways and highways are long, linear projects, certain requirements must be met in the detection and analysis of such objects: First, large area coverage is necessary because the lifelines and transportation networks have different directions and unified reference data are needed for monitoring, requiring large-scale synchronous measurement. Second, the lifeline serves the people over a long time and requires long-term, near real-time monitoring. The traditional geodetic deformation monitoring methods are mainly based on leveling and Global Positioning System (GPS) approaches. Traditional leveling is limited to discrete points on fixed routes. This approach is time consuming and expensive, so it is difficult to use for real-time monitoring. Although GPS technology can achieve high-precision monitoring, it is subject to the density of GPS points. The development of sequential InSAR technology provides a feasible technical means for real-time and long-term monitoring of long-standing linear engineering projects. At present, there are many studies on the application of InSAR technology to lifelines and transportation networks (Hung et al., 2010; Shan et al., 2012; Chen et al., 2012; Qin et al., 2016; Hoope et al., 2014; Wang et al., 2017; Yu et al., 2013). The French SNCF Institute (2008) used TS-DInSAR technology to analyze the deformation along the Paris-Amsterdam high-speed railway and verified the feasibility of this method. Gatti et al. (2010) used PS-InSAR technology to analyze the deformation of a railway in Italy over three years, which further proved the applicability of time series InSAR technology. Daniel et al. (2018) used InSAR technology to monitor the changes in highway bridges, which verified the feasibility of InSAR technology for monitoring lifelines and other facilities. Xing et al. (2018) improved the technical accuracy of PS-InSAR by installing angular reflectors, but the installation of angular reflectors requires manpower and materials and depends on the amount of SAR data generated by PS-InSAR technology.

At present, most of the lifeline monitoring is performed using PS-InSAR technology in order to overcome the disadvantage of PS-InSAR technology, which requires high data volume, and to improve the accuracy of deformation monitoring. In this paper, the InSAR method using the Full Rank Matrix (FRAM) Small Baseline Subset InSAR (SBAS) proposed by Li (2015) is used to study the deformation of the railway section from Lhasa to Nagqu. Using Advanced Synthetic Aperture Radar (ASAR) and TerraSAR-X data, the crustal deformation information of the Qinghai-Tibet Railway over 10 years (from planning to construction of the railway) was obtained and the relationship between crustal deformation and surrounding geological disasters was analyzed.

批注 [z3]: Reply to the comment 4 of RC1

批注 [z4]: Reply to the minor issue 2 of editor decision

2 Study area

The Qinghai-Tibet Railway is a high-elevation railway that connects Xining (Qinghai Province) to Lhasa (Tibet Autonomous Region) (Figure 1). The Qinghai-Tibet Railway and other national key projects that cross multiple active blocks and faults are vulnerable to earthquakes and other disasters (Chen et al., 2018; Wu et al., 2016). Thus, monitoring the deformation of these

projects is particularly important. InSAR and GPS are efficient techniques for monitoring the crustal deformation of Qinghai-Tibet blocks (Zhang et al., 2017).

The Qinghai-Tibet Railway, highway, transmission line and other national key projects, with their ancillary studies, have the characteristics of strong correlations and continuous long-distance distributions. It is important to understand how to use these features to monitor the deformation of a long, linear region and reveal the movement of the Qinghai-Tibet Plateau block patterns with the deformations of these major project networks.

The Lhasa-Nagqu section of the railway is located at the bottom of the southern valley of Nyainqentanglha Mountain in the central part of the Lhasa block (Jiang et al., 2018). In general, this section is north trending, and the Qinghai-Tibet Highway and Lhasa River pass through the area. Figure 2 shows the study area, and the base map is derived from a digital elevation model (DEM). The terrain in the area is undulating, with the Nyainqentanglha Mountain Range in the northwest, a mountainous area in the southeast, and the Yangbajing-Damxung Basin in the middle of the region (Wu et al., 2018). The terrain is flat, the Qinghai-Tibet Railway and Qinghai-Tibet Highway pass through the basin, and the vegetation along the railway is dense. Wetlands and low-lying regions are widely distributed, and the frozen soil in a long segment of the area contains abundant ice (Li et al., 2012). The study area is in a midlatitude region, and the land types mainly include glaciers, snow, bare rock and other land types. In this area, the Bengco fault lies across the railway; therefore, it is also important to study whether the movement of the Bengco fault affects the stability of the railway.

批注 [z5]: Reply to the comment 5 of RC1

3 Datasets and methodology

3.1 Datasets

The greatest feature of the railway is its long linear engineering; to monitor and analyze this type of ground object, certain requirements must be met. The first is large area coverage because the road direction is not the same everywhere and, in monitoring, the need for a unified reference standard requires large-scale synchronized measurements. Second, to meet the requirements of InSAR technology, such projects must apply a high-precision InSAR data processing algorithm to ensure high-resolution and fine-scale detection.

The TerraSAR-X data were acquired in stripmap mode with an incidence angle range of 39°-40° at HH polarization. The potential of the X-band data for detecting higher deformation gradients compared to that of other sensors arises from the high spatial and temporal resolutions of these data. Nevertheless, the coverage of the stripmap mode data is too small to study long, linear engineering projects. Therefore, in this paper, the C-band ASAR data and TerraSAR-X data were used in combination to analyze the stability of the Qinghai-Tibet Railway. The TerraSAR-X data were selected to verify the accuracy of the ASAR T405 data results over the first segment of the railway in Yangbajain, and the ASAR T133 data were used to analyze the deformation of the railway near the Nagqu area because the ASAR T405 data could not cover this area completely, and the ASAR T133 data could also verify the accuracy of the ASAR T405 data results over the Nagqu area. The data coverage is shown in Figure 2 with the blue dotted line.

The ASAR T405 data were acquired from August 2003 to September 2010, but there were no data for 2016; therefore, we processed the data in three stages (2003-2005, 2007, and 2008-2010). The ASAR T133 data were acquired from November 2007 to August 2010. The TerraSAR-X data were acquired from December 2011 to November 2012.

批注 [z6]: Reply to the comment 6 of RC1

3.2 Methodology

To minimize the spatial and temporal decorrelations, we constructed a baseline network (Figure 3) using the following criteria: perpendicular baselines shorter than 200 m and a daytime interval baseline of less than 180 days. Each acquisition node in the network has at least two link pairs, meaning that each node has a minimum number of connections with the other nodes (two are used in this paper).

Because of the change in the water vapor content in the atmosphere, phase artifacts in InSAR images caused by path delays, such as radar signal propagations through the stratified and turbulent atmosphere and ionosphere, frequently degrade the interpretability of the phase and correlation signatures of the terrain. The effect of atmospheric delay consists of three parts: 1) the long wavelength effect of the atmosphere, which is similar to the orbit error effect; 2) the short wavelength effect of the atmosphere (i.e., turbulent atmospheric artifacts); and 3) the vertical stratification of the atmosphere, which causes height-dependent refractivity variations. In this paper, the three phase delays are calculated using a network methodology. The methodology estimates the phase delay for each SAR acquisition; then, each atmospheric artifact is simulated. The proposed method can effectively eliminate the atmospheric phase delay in the interferograms.

The main steps of the FRAM-SBAS (Full Rank Matrix-Small Baseline Subset InSAR) method are as follows:

Firstly, the principle of interferogram generation is based on a specific time baseline and space baseline, and the appropriate redundant interferogram is selected to maximize the interferogram coherence. The main constraints are

$$\begin{cases} \left|\Delta B_{\perp}\right| < B_{\perp thr} \\ \left|\Delta t\right| < t_{thr} \\ \left|\Delta DC\right| < DC_{thr} \end{cases} \tag{1}$$

where $\Delta B_{\perp}$ is the vertical baseline of data interference pairs, Δt is the time baseline and ΔDC is the Doppler frequency difference.

Secondly, coherence points are selected. The coherence point is selected based on the principle of full rank matrix, which effectively improves the quality of coherent point selection and provides the basis for subsequent least squares inversion. By constructing a single set interferogram network, each point can construct the matrix described by Equation 1, where A is an $M * N$ dimensional matrix, M is the number of interferograms, and N is the number of images. For any pixel in any interferogram, the coherence is greater than a certain threshold, and the -1 and 1 flags can be set at the corresponding positions of the matrix A of Equation 1. For example, the first interferogram consists of the first image and the third image; that is, $\delta_{\phi 1}=\phi_3-\phi_1$. If the interference of a certain point in the interferogram satisfies the conditions, then the corresponding position

are $A_{11} = -1$ and $A_{13} = 1$, and the remaining positions of the first line are 0. Similarly, in the second interferogram, if the coherence of the point in one of the interferograms is less than the coherence threshold, the diversion is set to zero. All interferograms are considered to obtain each point pair matrix, and then the rank of each matrix is determined. If the matrix is full rank, the point is selected as the coherence point. The method can be used to select points that are coherent in the time series and coherent in the partial time interval but the interference network is connected, thereby increasing the number and precision of the coherent points.

$$A = \begin{bmatrix} -1 & 0 & 1 & \cdots & 0 & 0 & 0 \\ 0 & -1 & 1 & \cdots & 0 & 0 & 0 \\ & & \cdots\cdots\cdots\cdots & & & & \\ & & \cdots\cdots\cdots\cdots & & & & \\ 0 & 0 & 0 & \cdots & -1 & 1 & 0 \\ 0 & 0 & 0 & \cdots & -1 & 0 & 1 \end{bmatrix} \quad (2)$$

Thirdly, discrete point phase unwrapping is performed. In the FRAM-SBAS method, discrete coherence point data are resampled onto a regular Cartesian grid and phase unwrapping is performed using a network flow method. Then, the phase jump is checked according to the closed ring residual method, and the jump phase is corrected for the jump region.

Fourthly, orbital and atmospheric error removal is performed. The orbit error removal is performed using the network method proposed by Biggs et al. (2007). The atmospheric error is divided into long-wavelength atmospheric delay error and turbulent atmospheric delay error and terrain-related atmospheric delay error. The three errors are removed using the network methods. Traditional atmospheric delay phase (APS) estimates are based on a single interferogram (Ferretti et al., 2001). The atmospheric phase in the interferogram is the difference in atmospheric phase delay between the sub-image and the main image. If one of the two images is used to generate other interferograms, the phase delay signal on the image is also passed to the other interferograms, which also makes a correlation between the two interferograms. In this paper, we will use the network method to estimate the atmospheric delay error of each image acquisition time and then use these estimates to obtain the delay error of a single moment to reconstruct the atmospheric delay error of each interferogram.

After removal of the DEM error and the deformation phase, it can be assumed that the residual phase is mainly caused by the atmosphere. Suppose $\delta\varphi_j(x,y)$ represents the residual phase value at (x,y) on the jth interferogram and that $\varphi(t_A,x,y)$ and $\varphi(t_B,x,y)$ represent the phase values of the imaging moments t_A and t_B at (x,y), respectively. Each interferogram can be expressed by Equation (3):

$$\delta\varphi_j(\mathrm{x},\mathrm{y}) = \varphi(t_B,x,y) - \varphi(t_A,x,y) \quad (3)$$

Based on a short baseline set network, we can construct equations such as (4):

$$\boldsymbol{\delta\varphi = A * \varphi} \quad (4)$$

where $\boldsymbol{A}$ represents the $M * N$ matrix. The element A_{kl} of the matrix $\boldsymbol{A}$ is defined according to the following rules: If $l = t_B$, then $A_{kl} = 1$; if $l = t_A$, then $A_{kl} = -1$; otherwise, $A_{kl} = 0$. $\boldsymbol{\delta\varphi}$ is a known vector of M dimension, representing the number of interferograms M; $\boldsymbol{\varphi}$ is an N-dimensional unknown vector representing the atmospheric phase values of N imaging moments. Equation (4) can be rewritten as follows:

$$\begin{bmatrix} \delta\varphi_1(x,y) \\ \vdots \\ \delta\varphi_k(x,y) \end{bmatrix} = \begin{bmatrix} -1 & 0 & 1 & & \\ & \ddots & & \ddots & \\ & & 0 & -1 & 1 \end{bmatrix} \begin{bmatrix} \varphi^{t_0}(x,y) \\ \vdots \\ \varphi^{t_k}(x,y) \end{bmatrix} \quad (5)$$

where $\delta\varphi_k(x,y)$ represents the residual phase of interferogram k and the corresponding position is (x, y).

Since the matrix $\boldsymbol{A}$ is the rank-deficient matrix, a unique solution cannot be obtained. Generally, the singular value decomposition (SVD) method can be used to solve the solution and the atmospheric delay at each moment is obtained; then, the phase value of each interferogram is simulated by using Equation (5). In the calculation of the variance of the residual phase of each interferogram, if the interferogram has the lowest atmospheric variance, the atmospheric phase of the interferogram is assumed to be zero. This constraint is added to Equation (5) to calculate the atmospheric delay phase of all other image acquisition moments (Li et al., 2014).

Fifthly, the deformation result is obtained. The interference pattern is settled using the least squares method to obtain the deformation results of the study area.

The specific procedure is illustrated in Figure 4.

First, all selected SAR data along the vertical baseline are computed and the main image is selected. Second, redundant network interference and the raw SAR data are generated for a single look complex (SLC) image. Third, the appropriate DEM is selected, the DEM and SAR image are registered, and the interference subset is generated. Fourth, the data are resampled and the dataset is transformed into a unified coordinate system. Then, the full rank coherent matrix method is used to extract the full-rank permanent scatterers (PS) point and perform phase unwrapping and orbit error correction. Finally, the data are obtained based on the results of deformation rate time series.

4 Results and discussion

To remove the influence of far-field topography and Earth movement around the railway, the image was clipped to retain a certain area along the railway line. The SAR data before and after the opening of the railway were processed to obtain crustal deformation information along the railway.

批注 **[z7]:** Reply to the comment 1 of RC1

批注 **[z8]:** Reply to the comment 1 of RC2

4.1 InSAR results

The deformation information obtained by ASAR T405 during the construction of the Lhasa-Naqu section of the Qinghai-Tibet Railway from 2003 to 2005 is shown in Figure 5. The crust of this section is relatively stable: there is basically no deformation, and the maximum deformation is approximately 5 mm/yr.

In 2007, the Lhasa-Naqu section of the Qinghai-Tibet Railway was functionally completed and opened to traffic. Figure 6 shows the deformation information of the line obtained by ASAR T405 in 2007. The area of the line is obviously variable compared with that before the opening of the railway. In the area circled by the elliptical red dotted line, the deformation is large, with a maximum value of 20 mm/yr. The operation of the train has a certain impact on the railway, which may because the roadbed bears the weight of the train, causing the roadbed to become compacted and sink.

From 2008 to 2010, three years after the smooth operation of the Qinghai-Tibet Railway, the deformation of the line slowed compared with that in 2007 (Figure 7). The main deformation area is consistent with the deformation zone in 2007, mainly in the area of Damxung, which may be due to the geothermal exploitation in the area. A comparison of ASAR T405 and ASAR T133 reveals that the maximum deformation in this area is 15 mm/yr. However, the deformation in the northern part of the railway is relatively stable.

The overlap area between TerraSAR-X and ASAR is located above Yangbajing, and the deformation field obtained from the two datasets is analyzed. Figure 8(A) indicates that the ASAR acquired the deformation field in the region from 2008 to 2010. There is an obvious uplift area at the corner of the railway from 2008 to 2010, and the maximum cumulative uplift is up to 7 mm/yr. Figure 8(B) shows the deformation field acquired by TerraSAR-X from 2011 to 2013, and the deformation of the uplift area at the corner is obviously smaller and tends to be stable, but there are two subsidence areas in the lower left corner and upper right corner, where the maximum subsidence is 10 mm/yr. The reasons for the subsidence area are analyzed by superposing geological hazards.

For the present analysis, a section of the railway in Damxung is selected (Figure 9). In 2003-2005, the section of the road surface was basically stable; in 2007, the construction of the railway resulted in a region with a large area of settlement, where the maximum settlement rate was 20 mm/yr. In 2008-2010, the subsidence area was reduced, and the maximum settlement rate was 10 mm/yr; the surface tended to be stable.

Based on the results of the deformation field obtained for 2009-2010, some high-voltage towers along the Lhasa-Naqu railway are analyzed (Figure 10). The results show that different sections of the towers have different drops or lifts. The maximum lifting capacity of D306 is 17 mm, and the maximum settlement of D269 is 18 mm. Most of the larger variables are located at the corner of the railway and within a section of the line.

In this paper, the SAR data from 2003 to 2012 are analyzed. It is concluded that during the construction of the Qinghai-Tibet Railway, the linear variable along the railway was approximately 10 mm/yr. After the completion of the traffic, the linear variable along the railway was 4-8 mm/yr. Li et al. (2012) used SBAS technology to analyze the ENVISAT ASAR data from 1997 to 2010 in the vicinity of Yangbajing-Dangxiong of the Qinghai-Tibet Railway. It was found that the settlement rate near

the railway was 2 mm/yr, and the impact of frozen soil was approximately 10 mm/yr. Zhang et al. (2017) used Sentinel-1 data to analyze the deformation variables of the Qinghai-Tibet Railway during the period of 2014-2016 in the Qinghai-Tibet Plateau. It is concluded that the settlement rate of the Qinghai-Tibet Railway is approximately -10 mm/yr and the settlement rate of the rail-stabilized area is approximately -5 mm/yr. Ma et al. (2011) and Dong et al. (2013) found that the overall settlement rate of the Qinghai-Tibet Railway subgrade is <10 mm/yr. At the junction of the fracture, we verified this finding with GPS, and the GPS result was highly consistent with the deformation field acquired by InSAR. Chen et al. (2012) used C- and L-band small baseline SAR interferometry to analyze the interaction between permafrost and infrastructure along the Qinghai-Tibet Railway, and the results showed surface motions along the embankment primarily in the range of - 20 to + 20 mm/yr.

批注 [z9]: Reply to the comment 2 of RC1

4.2 Deformation and hazards

The Qinghai-Tibet Railway runs along the Qinghai-Tibet Plateau and its eastern margin. Under the influence of the uplift of the Qinghai-Tibet Plateau, the topography is generally high in the west and low in the east. The Qinghai-Tibet Railway passes through structural units, such as the modified Nagqu orogenic belt and the Lhasa block. The climatic region of the Qinghai-Tibet Plateau has obvious vertical zoning characteristics, large temperature differences between winter and summer, and strong freeze-thaw weathering, which makes the geological environment along the Qinghai-Tibet Railway and adjacent areas sensitive and conducive to the development and occurrence of geological disasters.

In this paper, the upper Yangbajing railway section is selected and the geological hazard and deformation fields are superimposed (Figure 11). The geological hazards occur mostly in areas with large deformation fields, which are also in the corner along the railway. There is basically no distribution of geological hazard points in the stable area of the deformation field, which shows that the stability of the surrounding geological structure is affected by railway construction and other factors, resulting in frequent geological hazards. At the same time, to ensure the safe and normal operation of the railway, it is necessary to perform long-term monitoring of the geological and geomorphological conditions around the railway to avoid casualties and economic losses.

4.3 Deformation and the Bengco fault

Garthwaite et al. obtained the deformation field within the Qinghai-Tibet Plateau by using large-scale InSAR technique. The present slip rate of the Bengco fault is 1-4+1 mm/yr. At 90.30°E, the slip rate is 1 mm/yr, which is 40 km west of the rupture zone of a 1951 earthquake. At 90.75°E, which is located in the western part of the rupture zone, the sliding rate reaches 4 mm/yr (Garthwaite et al., 2013). Ryder also used the InSAR method to estimate the deformation rate of the Bengco fault. The right-lateral slip deformation at 90.4°E is approximately 1 ± 1 mm/yr, and that at 90.9°E is approximately 4 ± 1 mm/yr. It is believed that this fracture deformation is mainly caused by the post-earthquake stick-slip effect of two earthquakes in 1951 and 1952 (Ryder et al., 2014). Taylor et al. studied a series of V-shaped conjugate tectonic belts using the InSAR technique. The present slip rates of several tectonic belts in the central and western regions are consistent with GPS results (Taylor et al., 2006).

Using the 32 ASAR image scenes between 2004 to 2010 (two adjacent tracks, T176 and T405) (Figure 12), the same treatment method as described in Section 3.2 was used to obtain the deformation rate of the Bengco fault zone. Three section lines, A-A', B-B', and C-C', are selected in the deformation rate map to analyze the slip rate of the Bengco fault (Figure 13). It can be seen from the results that the formation rate of the Bengco area is between 1 and 3 mm/yr. The rate in the eastern segment is approximately 2-3 mm/yr, and that in the western segment is approximately 1-2 mm/yr. The intersection of the A-A' section line and the fault essentially coincides with the intersection of the Qinghai-Tibet Railway and the fault-breaking fault zone. From the results of the section deformation rate, it can be seen that the fault slip has little effect on the overall deformation of the railway.

5 Conclusions

We used FRAM SBAS technology to measure deformation rates in the Lhasa Nagqu railway section using 49 ASAR image scenes and 17 TerraSAR-X SAR image scenes collected between August 2003 and November 2012. Due to the lack of data for 2006, we divided the data into five groups. The two datasets can provide detailed deformation information on the Qinghai-Tibet Railway. The main conclusions of this work can be summarized as follows.

(1) Before the opening of the railway, the Qinghai-Tibet Railway deformation was very small and the roadbed was considered stable. During the period of operation after the completion of the railway, the roadbed was relatively unstable during the first two or three years, and different subsidence and uplift zones appeared along the railway. During the later stage, with the accumulation of running time, the road surface gradually stabilized and the shape variations gradually decreased.

(2) The whole railway is relatively stable. The influence of frozen soil around the railway is affected by surface deformation, but, in general, this condition is not very serious. However, through the analysis of geological hazards and deformation fields, segments where the deformation field changes greatly are more likely to experience geological disasters, and geological disasters and abnormal deformations most commonly occur at the corner of the railway. Therefore, it is necessary to conduct real-time deformation and geological hazard monitoring along the Qinghai-Tibet Railway.

(3) To ensure the sustainable development of the Qinghai-Tibet Railway, the following analyses are urgently needed. First, the continuous monitoring of ground surface subsidence near the Qinghai-Tibet Railway and surrounding regions must be carried out using a geodetic survey (e.g., GPS and InSAR). Second, the distribution of geological hazards along the Qinghai-Tibet Railway and the regional geological structure need to be analyzed in detail. Finally, for the long-term regional monitoring of InSAR data, the splicing of different orbital data and the processing of massive data are also key problems that need to be solved.

References

Altamira-information. Case study: monitoring of high speed line (SNCF). 2008. http://www.altamira-information.com/html-18637-CASE-STUDY-Monitoring-of-high-speed-line-SNCF.php

Berardino, P., Fornaro, G., Lanari, R., and Sansosti, E.: A New Algorithm for Surface Deformation Monitoring Based on Small Baseline Differential SAR Interferograms, Geoscience and Remote Sensing, IEEE Transactions, 40(11), 2375-2383, doi: 10.1109/TGRS.2002.803792, 2002.

Brown, J., Hinkel, K.M., and Nelson, F.E.: The Circumpolar Activelayer Monitoring (CALM) Program: Research Designs and Initial Results, Polar Geography, 24 (3), 166-258, doi: 10.1080/ 10889370009377698, 2000.

Chang, Z. Q., Liu, X. M., Xue, T. F., and Yang, R. R.: Investigating ground subsidence in Beijing by using interferogram stacking InSAR, IEEE International Conference on Spatial Data Mining & Geographical Knowledge Services, IEEE, doi: 10.1109/ICSDM.2011.5969068, 2011.

Chen, F. L., Lin, H., Li, Z., and Zhou, J. M.: Interaction between permafrost and infrastructure along the Qinghai-Tibet Railway detected via jointly analysis of C- and L-band small baseline SAR interferometry, Remote Sensing of Environment, 123(8), 532-540, doi:10.1016/j.rse.2012.04.020, 2012.

Chen, T., Ma, W., and Zhou, G.: Numerical analysis of ground motion characteristics in permafrost regions along the Qinghai-Tibet Railway, Cold Regions Science & Technology, 148, 88-95, https://doi.org/10.1016/j.coldregions.2018.01.016, 2018.

Corsetti, M., Fossati, F., Manunta, M., and Marsella, M.: Advanced SBAS-DInSAR technique for controlling large civil infrastructures: An Application to the Genzano di Lucania Dam, Sensors, 18(7), doi: 10.3390/s18072371, 2018.

Dai, K. R., Liu, G. X., Li, Z. H., Ma, D. Y., Wang, X. W., Zhang, B., Tang, J., and Li, G. Y.: Monitoring Highway Stability in Permafrost Regions with X-band Temporary Scatterers Stacking InSAR, Sensors, 18(6), 1-17, doi: 10.3390/s18061876, 2018.

Daniel, C., Ken, T., Hébert, D., Glenn, H., Matthew, G., and Parwant, G.: Satellite-Based InSAR Monitoring of Highway Bridges: Validation Case Study on the North Channel Bridge in Ontario, Canada, Transportation Research Record: Journal of the Transportation Research Board, 45(2672), 76-86, doi: 10.1177/0361198118795013, 2018.

Dong S. C., Samsonov, S., Yin, H. W., Ye, S. J., and Cao, Y. R.: Time-series analysis of subsidence associated with rapid urbanization in Shanghai, China measured with SBAS InSAR method, Environmental Earth Sciences, 72(3), 677-691, doi: 10.1007/s12665-013-2990-y, 2014.

Dong, Shaochun., Sergey, S., Hongwei, Y., Shujun, Y., and Yanrong, C.: Time-series analysis of subsidence associated with rapid urbanization in shanghai, china measured with sbas insar method, Environmental Earth Sciences, 72(3), 677-691, 2014.

Dong, C. H., and Zhao, X. Q.: Analysis on subgrade deformation features and influence factors in permafrost regions on Qinghai-Tibet Railway, Railway Standard Design, 6: 5-8, 2013.

Ferretti, A.: Nonlinear subsidence rate estimation using permanent scatters in differential SAR interferometry, IEEE Transactions on Geoscience & Remote Sensing, 38(5), 2202-2212, doi: 10.1109/36.868878, 2000.

Ferretti, A.: Permanent scatterers in SAR interferometry, IEEE Transactions on Geoscience & Remote Sensing, 39 (1), 8-20, doi: 10.1109/36.898661, 2001.

Gabriel, A.K., Goldstein, R.M., and Zebker, H.A.: Mapping small elevation changes over large areas: Differential radar interferometry, Journal of Geophysical Research: Solid Earth (1978-2012), 94(B7), 9183-9191, doi: 10.1029/JB094iB07p09183, 1989.

Gatti, G., Wang, T., and Perissin, D.: Railways monitoring by means of repeated space-borne SAR images, Spatial Information Technologies for Monitoring the Deformation of Large-Scale Man-made Linear Features, Hong Kong, China. 11-12 January 2010.

Garthwaite, M.C., Wang, H., and Wright, T.J.: Broadscale interseismic deformation and fault slip rates in the central Tibetan Plateau observed using InSAR, Journal of Geophysical Research Solid Earth, 118(9), 5071-5083, doi: 10.1109/TGRS.2009.2019125, 2013.

Guodong, C.: Constructing of the Qinghai-Tibet Railroad using the principle of cooling the roadbed, China Railway Science, 24(3): 1-4, 2003.

Han, Y. F., Song, X. G., Shan, X. J., Qu, C. Y., Wang, C. S., Guo, L. M., Zhang, G. F., and Liu, Y. H.: Deformation monitoring of Changbaishan Tianchi voleano using D-InSAR technique and error analysis, Chinese journal of geophysics, 53(7), 1571-1579, 2010.

Hoppe, E., Bruckno, B., Acton, S., and Bohane, A.: Transportation Infrastructure Monitoring Using Satellite Remote Sensing, Materials and Infrastructures 1, John Wiley & Sons, Inc, doi: 10.1002/9781119318583.ch14, 2014.

Hu, M.J., Wang, R., Tan, S. L., and Shi, X. F.: Development of drill monitoring instrument for frozen soil settlement, Rock and Soil Mechanics, 28(10), 2215-2218, 2007.

Hung, W. C., Hwang, C., Chang, C. P., Yen, J. Y., Liu, C. H., and Yang, W. H.: Monitoring severe aquifer-system compaction and land subsidence in taiwan using multiple sensors: yunlin, the southern choushui river alluvial fan, Environmental Earth Sciences, 59(7), 1535-1548, 2010.

Jiang, Y., Gao, Y., Dong, Z. B., Liu, B. L., and Zhao, L.: Simulations of wind erosion along the Qinghai-Tibet Railway in north-central Tibet, Aeolian Research, 32, 192-201, https://doi.org/10.1016/j.aeolia.2018.03.006, 2018.

Jin, H. J., Yu, Q. H., Wang, S. L., and Lv, L. Z.: Changes in Permafrost Environments along the Qinghai-Tibet Engineering Corridor Induced by Anthropogenic Activities and Climate Warming, Cold Regions Science and Technology, 53, 317-333, doi: 10.1016/j.coldregions.2007.07.005, 2008.

L, Zhao., Wu, Q. B., Marchenko, S. S., and Sharkhuu, N.: Thermal State of Permafrost and Active Layer Incentral Asia during the International Polar Year, Permafrost and Periglacial Processes, 21, 198–207, doi: 10.1002/ppp.688, 2010.

Li, S. S.: The study of using SBAS to monitor the Motion of the frozen soil along Qinghai-Tibet railway, Central south university, 2012.

Li, Y. S., Tian, Y. F., Li, Z. H., Zhang, J. F., Luo, Y., and Jiang, W. L.: Measurement ofsubsidence in the yangbajing geothermal fields, tibet, from terrasar-x insartime series analysis. International Journal of Digital Earth, International Journal of Digital Earth, 9(7), 697-709, 2016.

Li, Y. S., Zhang, J. F., Luo, Y., Jiang, W. L., and Liu, Z. M.: Monitoring of Surface Deformation In Dangxiong Using Time Series Analysis Techniques, Journal of Applied Geodesy, 6(3-4), 215-220, 2010.

Li, Y. S.: Surface Deformation Co-seismic and Post-seismic Activity Constrained by Advanced InSAR Time Series Analysis, Institute of Engineering Mechanics,China EarthquakeAdministration, Harbin, 2014.

Li, Z. H., Fielding, E.J., and Cross, P.: Integration of In SAR time-series analysis and water-vapor correction for mapping postseismic motion after the 2003 Bam (Iran) earthquake, Geoscience and Remote Sensing, 47(9), 3220-3230, 2009.

Liu, J. K., Bao, W. M., Han, X. G., and Bao, L. M.: Observation and analysis of a new type embankment-bridge transition section in permafrost regions, Journal of Glaciology and Geocryology, 26(6), 800-805, doi: 1000-0240(2004)06-0800-06, 2004.

Liu, Y. Z., Wu, Q. B., and Zhang, J. M.: Study on ground temperature field in permafrost regions of Qinghai-Tibet Plateau, Highway, 2, 4-8, 2000.

Lundgren, P., Usai, S., Sansoti, E., Lanari, R., Tesauro, M., Fornaro G., and Berardino, P.: Modelling surface deformation observed with synthetic aperture radar interferometry at Campi Flegrei caldera, Journal of Geophysical Research, 106 (B9), 19355–19366, doi: 10.1029/2001jb000194, 2001.

Ma, W., Liu, D., and Wu, Q. B.: Monitoring and analysis of embankment deformation in permafrost regions of Qinghai-Tibet Railway, Rock Mechanics, 29(3): 571-580, 2008.

Ma, W., Mu, Y. H., and Wu, Q. B.: Characteristics and mechanisms of embankment deformation along the Qinghai-Tibet Railway in permafrost regions, Cold Regions Science and Technology, 67(3): 178-186, 2011.

Ma, W., Mu, Y., Wu, Q., Sun, Z., and Liu, Y.: Characteristics and Mechanisms of Embankment Deformation along the Qinghai–Tibet Railway in Permafrost Regions, Cold Regions Science and Technology, 67, 178-186, doi: 10.1016/j.coldregions.2011.02.010, 2011.

Qin, X., Yang, M., Wang, H., Yang, T., and Liao, M.: Application of high-resolution ps-insar in deformation characteristics probe of urban rail transit, Acta Geodaetica et Cartographica Sinica, 45(6), 713-721, doi: 10.11947/j.AGCS.2016.20150440, 2016.

Rosi, A., Tofani, V., Tanteri, L., Tacconi, S. C., Agostini, A., Catani, F., and Casagli, N.: The new landslide inventory of Tuscany (Italy) updated with PS-InSAR: geomorphological features and landslide distribution, Landslides, 15(1), 5-19, doi: 10.1007/s10346-017-0861-4, 2017.

Ryder, I., Wang, H., Bie, L., and Rietbrock, A.: Geodetic imaging of late postseismic lower crustal flow in Tibet, Earth & Planetary Science Letters, 404, 136-143, doi: 10.1016/j.epsl.2014.07.026, 2014.

Shan, W., Wang, C. J., and Hu, Q.: Expressway and Road Area Deformation Monitoring Research Based on InSAR Technology in Isolated Permafrost Area, International Conference on Remote Sensing, IEEE, 1-5, doi: 10.1109/RSETE.2012.6260574, 2012.

Taylor, M., and Peltzer, G.: Current slip rates on conjugate strike-slip faults in central Tibet using synthetic aperture radar interferometry, Journal of Geophysical Research Solid Earth, 111, B12402, doi:10.1029/2005JB004014, 2006.

Wang, C., Liu, Z., Zhang, H., and Shan, X. J.: Differential interferometry for the same seismic deformation field of Shangyi - Zhangbei earthquake, Chinese Science Bulletin, 45(23), 2550-2554, 2000.

Wang, C., Zhang, Z. J., Zhang, H., Wu, Q. B., Zhang, B., and Tang, Y. X.: Seasonal deformation features on Qinghai-Tibet railway observed using time-series InSAR technique with high-resolution TerraSAR-X images, Remote Sensing Letters, 8(1), 1-10, doi: org/10.1080/2150704X.2016.1225170, 2017.

Welk, J.E.: Railway Crossing Collision Avoidance System, U.S. Patent, 5, 699-986, 23, 1997.

Wu, Q. B., and Zhang, T. J.: Recent permafrost warming on the Qinghai-Tibetan Plateau, Journal of Geophysical Research, 113, 1-22, doi: 10.1029/2007JD009539, 2008.

Wu, Q. B., Cheng, G. D., and Ma, W.: The impact of climate warming on Qinghai-Tibetan Railroad, Science in China, 47, 122-130, doi: 10.3969/j.issn.1673-1719.2008.z1.012, 2004.

Wu, Z. J., Ma, W., Chen, T., and Wang, L.: Dynamic Stability Analysis of Embankment along the Qinghai-Tibet Railroad in Permafrost Regions, Environmental Vibrations and Transportation Geodynamics, 757-766, doi: 10.1007/978-981-10-4508-070, 2016.

Wu, Z. W., and Liu, Y. Z.: Frozen soil foundation and engineering construction, Beijing: The Ocean Publishing Company, 142–146, 2005.

Wu, Z., Chen, T., Zhao, T., and Wang, L. L.: Dynamic response analysis of railway embankments under train loads in permafrost regions of the Qinghai-Tibet Plateau, Soil Dynamics & Earthquake Engineering, 112, 1-7, doi: org/10.1016/j.soildyn.2018.04.047, 2018.

Xing, X., Wen, D., Chang, H. C., Chen, L. F., and Yuan, Z. H.: Highway Deformation Monitoring Based on an Integrated CRInSAR Algorithm-Simulation and Real Data Validation, International Journal of Pattern Recognition and Artificial Intelligence, 32(11), 1-19, doi: 10.1142/S0218001418500362, 2018.

Xuzhi, Z., and Xinghua, W.: Deformation characteristics of culverts in permafrost regions of Qinghai-Tibet Railway, Hydrogeology & Engineering Geology, 2, 55-58, 2007.

Yang, C., Lu, Z., Zhang, Q., Zhao, C. Y., Peng, J. B., and Ji, L. Y.: Deformation at longyao ground fissure and its surroundings, north China plain, revealed by ALOS PALSAR PS-InSAR, International Journal of Applied Earth Observation and Geoinformation, 67, 1-9, doi: org/10.1016/j.jag.2017.12.010, 2018.

Yu, B., Liu, G., Zhang, R., Jia, H., Li, T., and Wang, X.: Monitoring subsidence rates along road network by persistent scatterer sar interferometry with high-resolution terrasar-x imagery, Journal of Modern Transportation, 21(4), 236-246, doi: 10.1007/s40534-013-0030-y, 2013.

Zhang, Z. J.: Research on Qinghai-Tibet Permafrost Environment and Engineering using High Resolution SAR Images, Institute of Remote Sensing and Digital Earth, Chinese Academy of Science, 2017.

批注 [z10]: Reply to the comment 3 of RC1 and comment 3 of RC2 and minor issue of editor decision

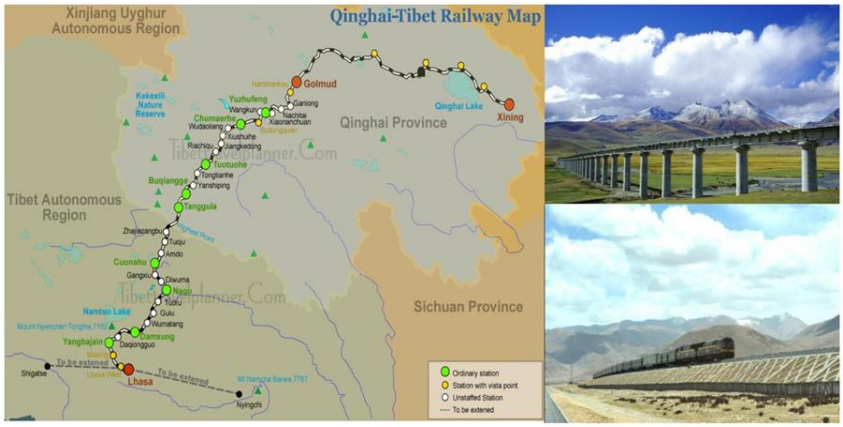

Figure 1. Qinghai-Tibet Railway

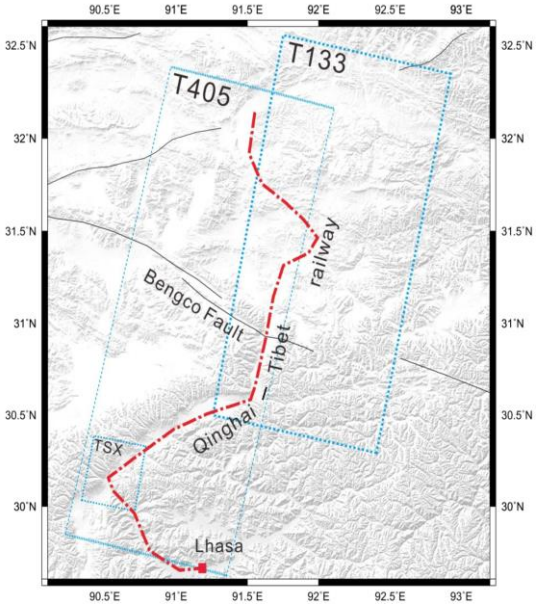

Figure 2. Study area and the distribution of the SAR imagery. The blue dotted line shows the extents of the ASAR and TerraSAR-X images. The red dotted line shows the railway. The black line shows the main fault in this area.

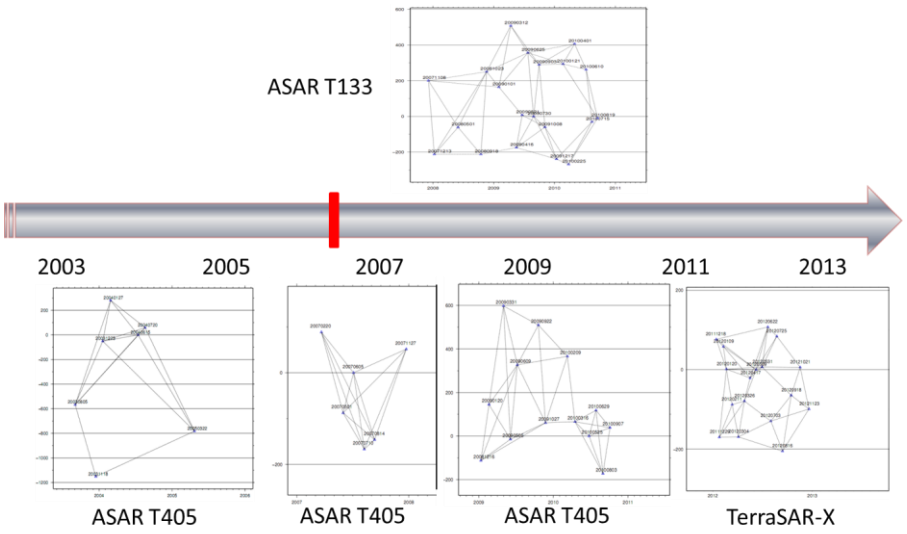

Figure 3. Temporal and perpendicular baselines for the interferograms used in this study. Different graphs represent the baselines of different data generated during different time periods.

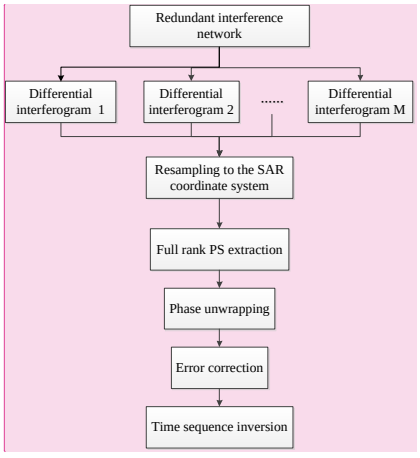

Figure 4. Process flow

批注 [z11]: Reply to the comment 7 of RC1

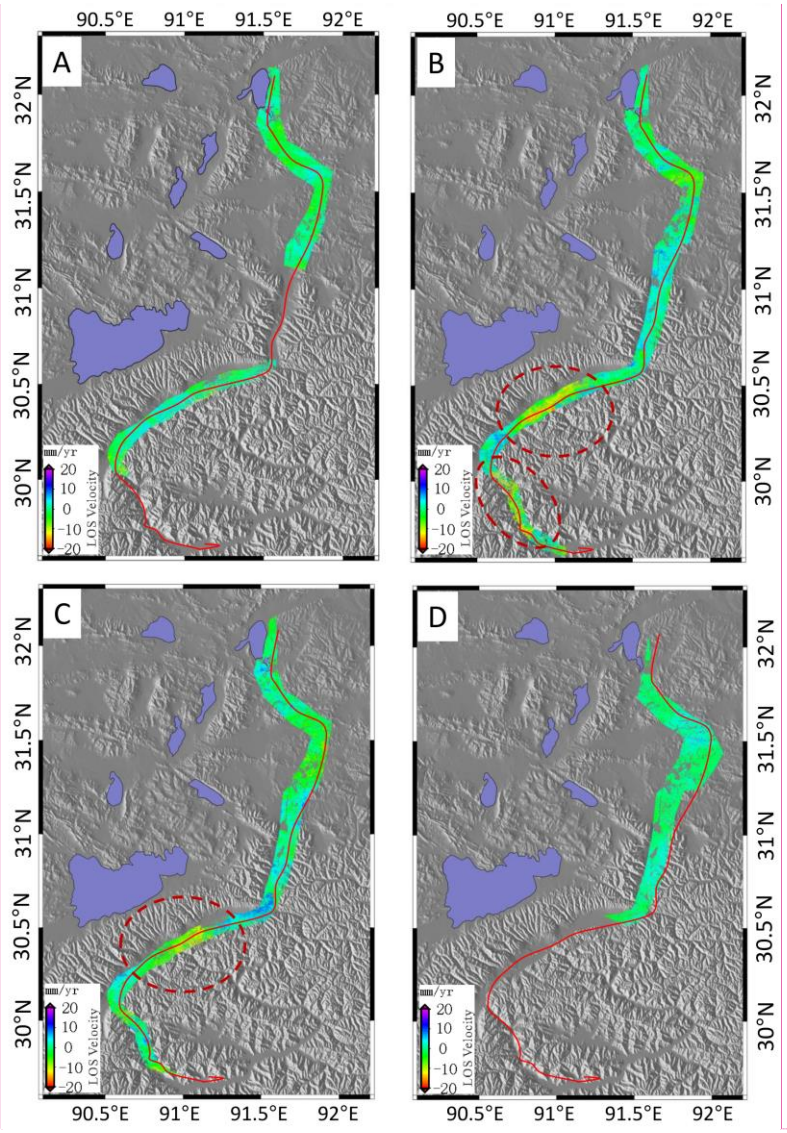

批注 [z12]: Reply to the comment 8 of RC1

Figure 5. The ASAR T405 results for the Lhasa-Naqu section of the Qinghai-Tibet Railway between 2003 and 2005. The red line represents the railway.

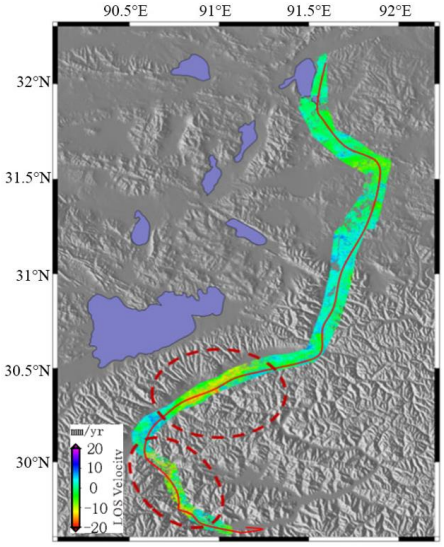

Figure 6. ASAR T405 results for the Lhasa-Naqu section of the Qinghai-Tibet Railway in 2007. The red line represents the railway. The elliptical red dotted line represents the region of large deformation.

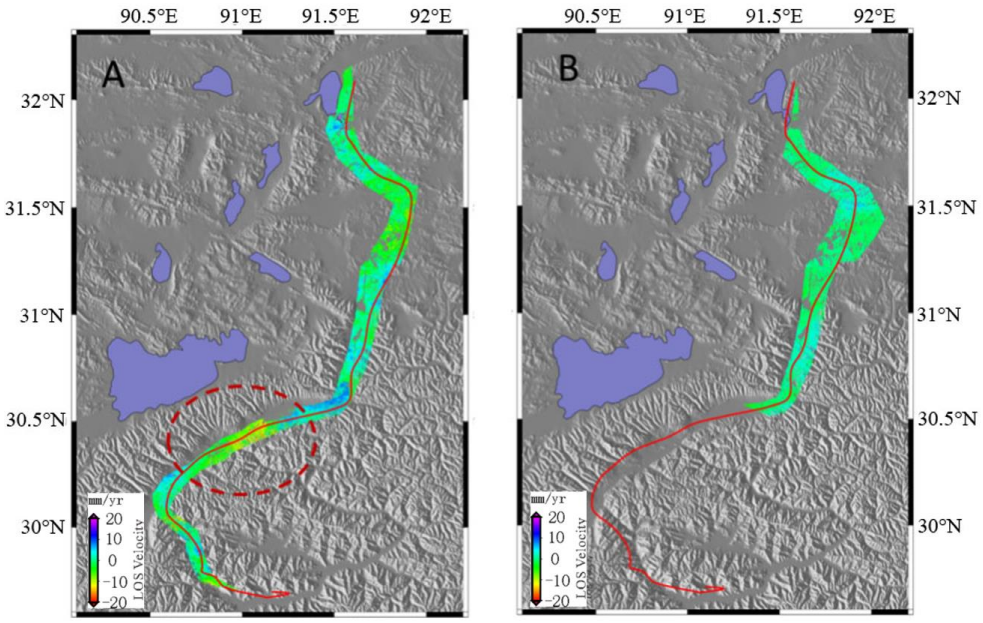

Figure 7. Deformation maps within three years after operation of the railway. (A) The data are ASAR T405 data from 2008 to 2010. (B) The data are ASAR T133 data from 2008 to 2010. The red line represents the railway.

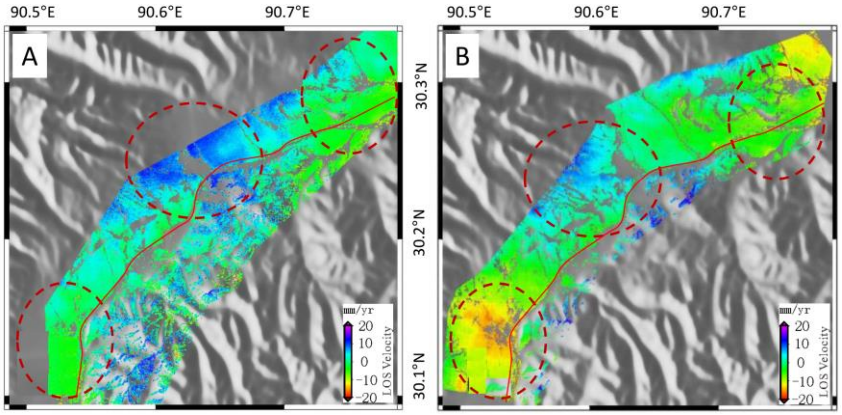

Figure 8. The deformation maps of the overlap area of the TerraSAR-X and ASAR data. (A) The ASAR T405 data range from 2008 to 2010. (B) TerraSAR-X data range from 2011 to 2012.

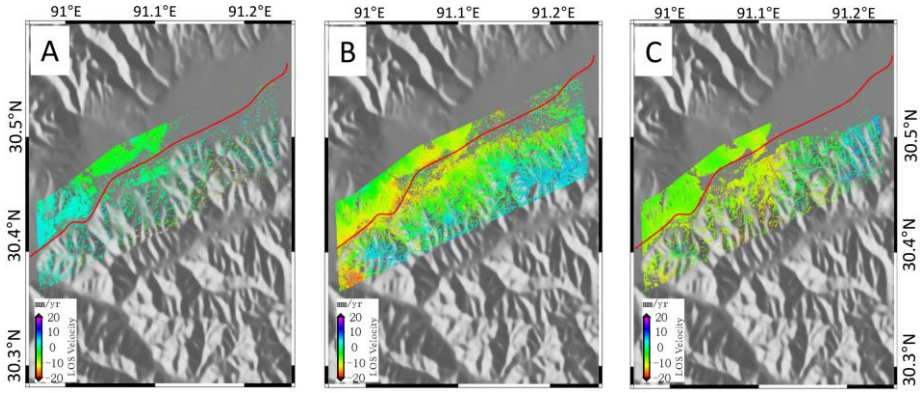

Figure 9. The deformation maps of the railway sequence changes from 2003 to 2010 in the Damxung section.

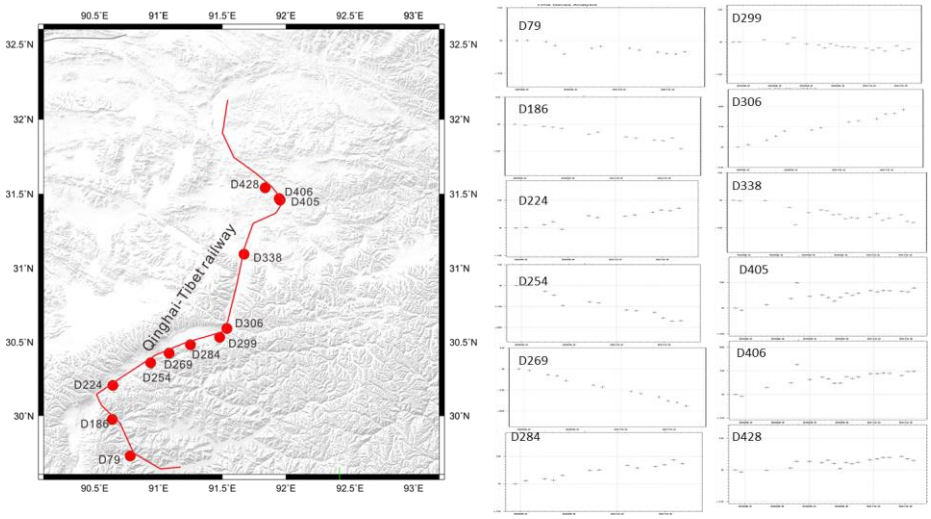

Figure 10. Deformation of a high-voltage power tower. (A) The location of the power tower. (B) The sequence of the deformation characteristics of the power tower.

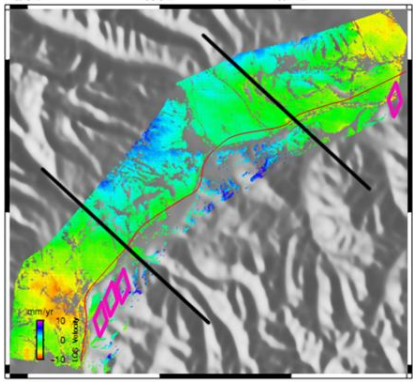

Figure 11. Deformation and hazards. The magenta rhombi show the geological hazard points.

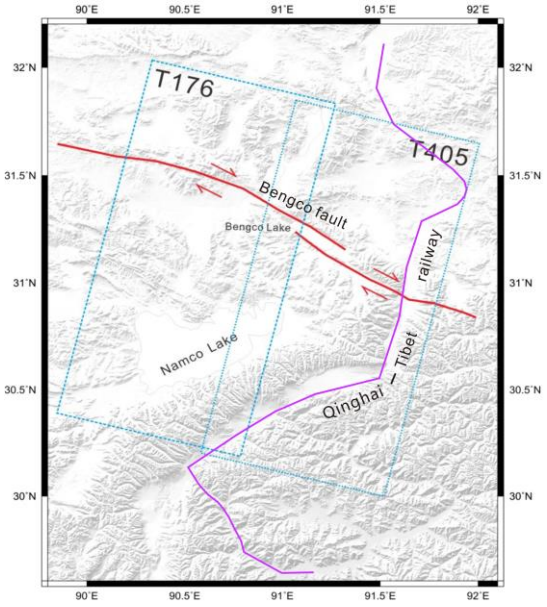

Figure 12. Bengco fault and the distribution of the SAR imagery. The blue dotted line shows the extents of the ASAR images. The red line shows the Bengco fault. The purple line shows the railway.

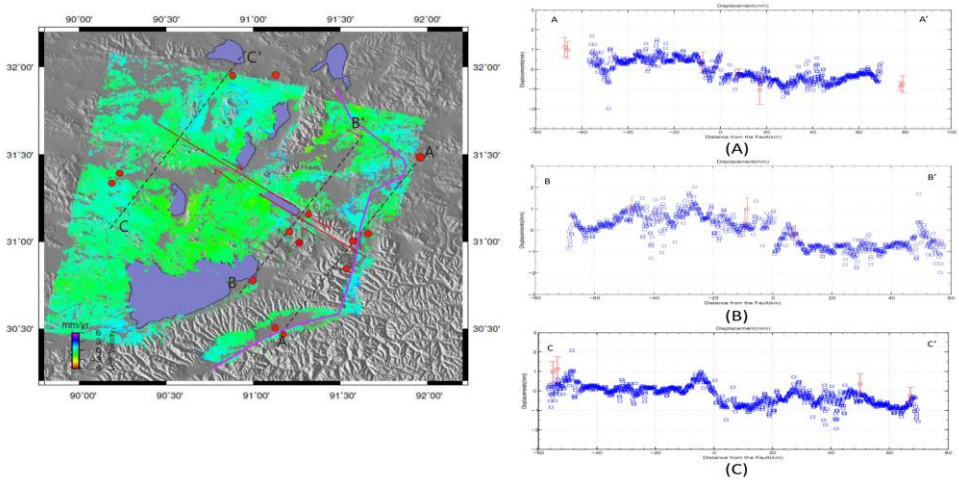

Figure 13. Bengco fault slip rate. The red line shows the Bengco fault. The purple line shows the railway. The red circle shows the GPS location. The black dotted line shows the section lines of the Bengco fault. The purple line shows the highway. The left figure shows the Bengco fault slip rate. The right figure shows the detailed information on section lines.